Volume 18
Number 1
7 January 2025
Pages 1–494

Energy & Environmental Science

rsc.li/ees

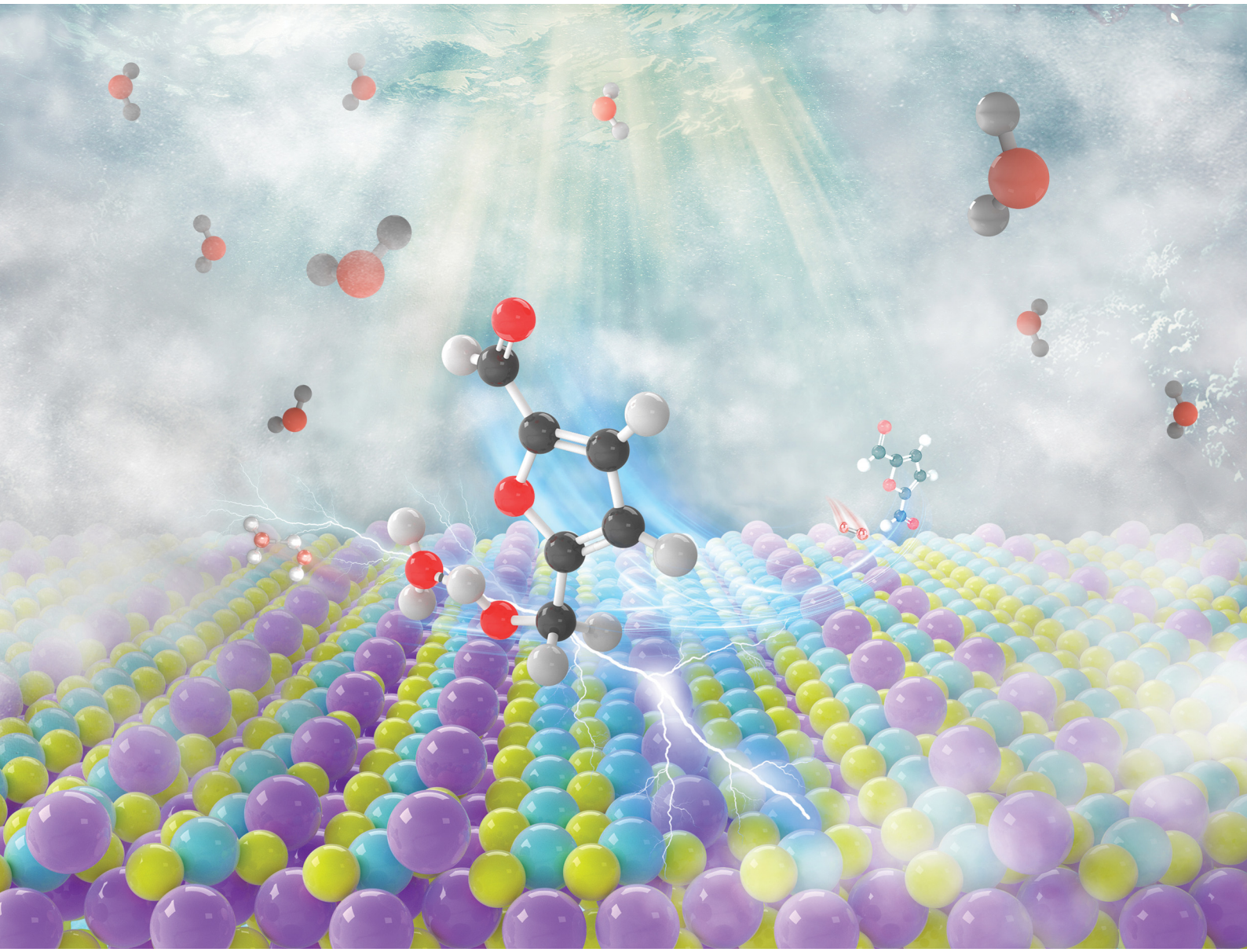

ISSN 1754-5706

ROYAL SOCIETY OF CHEMISTRY

PAPER

Jun Zhao *et al.*

Harnessing trace water for enhanced photocatalytic oxidation of biomass-derived alcohols to aldehydes

Energy & Environmental Science

ROYAL SOCIETY OF CHEMISTRY

PAPER

View Article Online
View Journal | View Issue

Cite this: *Energy Environ. Sci.*, 2025, **18**, 214

Harnessing trace water for enhanced photocatalytic oxidation of biomass-derived alcohols to aldehydes†

Wenhua Xue,[a] Jian Ye,[a] Zhi Zhu,[a] Reeti Kumar[a] and Jun Zhao *[ab]

Received 27th May 2024,
Accepted 16th September 2024

DOI: 10.1039/d4ee02301c

rsc.li/ees

The photocatalytic conversion of biomass into valuable chemicals offers a more energy-efficient and low-carbon alternative to traditional thermal catalysis, representing a promising strategy for fine chemical production without relying on fossil fuels. While most studies have focused on catalyst design to improve efficiency, the precise tuning of solvents has been neglected. This study examines the conversion of 5-hydroxymethylfurfural (HMF) into 2,5-diformylfuran (DFF) as a representative biomass alcohol oxidation reaction, revealing a novel strategy for enhancing photocatalytic efficiency through solvent fine-tuning. The introduction of minute quantities of water into an acetonitrile solvent matrix during the HMF oxidation reaction was observed to engender pronounced enhancements in catalytic performance, with the degree of effect contingent on precise water concentration. Trace water is an active participant in the catalytic cycle, diminishing the activation energy barrier for bond cleavage and averting catalyst deactivation. This mechanism also proved applicable to other photocatalysts and various alcohol substrates, highlighting the potential of this strategy for enhancing photoenergy utilization and reaction efficiency.

Broader context

This work on the photocatalytic conversion of biomass into valuable chemicals represents a significant advancement in the field of energy and environmental science. The study introduces a novel strategy for enhancing photocatalytic efficiency by focusing on the precise tuning of solvents in addition to catalyst design. Specifically, the discovery that the introduction of minute quantities of water into solvents can greatly improve catalytic performance offers a promising avenue for increasing the efficiency of biomass alcohol oxidation reactions. This finding not only sheds light on the underlying mechanisms at play during photocatalysis but also demonstrates a versatile approach that can be applied to various photocatalysts and alcohol substrates. The ability to lower activation energy barriers and prevent catalyst deactivation through the involvement of trace water in the catalytic system represents a significant step forward in the quest for sustainable and efficient chemical production from biomass feedstock.

Introduction

The catalytic transformation of biomass is pivotal in renewable energy and resource utilization, offering a strategy to lessen the dependence on fossil fuels and curb environmental pollution.[1–4] In contrast to traditional energy-intensive industrial processes, solar-driven biomass conversion has emerged as a promising approach for the sustainable production of high-value liquid-phase chemicals, characterized by its low energy consumption and minimal environmental footprint. Therefore, converting biomass alcohols into aldehydes is particularly valuable and industrially important since aldehydes serve as critical intermediates in producing fine chemicals and polymer precursors. However, the mechanism underlying the photocatalytic oxidation of these alcohols in the liquid phase remains largely obscure owing to the susceptibility of the catalytic activity of catalysts to reaction conditions (solvents and atmosphere). Therefore, a clear understanding of such photo-induced reactions is critical for advancing these industrial processes as it promises to reduce the dependence on fossil fuels in traditional chemical production and associated pollutant emissions, thereby achieving waste valorization in a more sustainable way.

As a representative biomass-derived chemical, the oxidation of 5-hydroxymethylfurfural (5-HMF) to 2,5-diformylfuran (DFF)

[a] *Department of Biology, Hong Kong Baptist University, Kowloon Tong, Hong Kong SAR, China. E-mail: zhaojun@hkbu.edu.hk*
[b] *Institute of Advanced Materials, Hong Kong Baptist University, Kowloon Tong, Hong Kong SAR, China*

† Electronic supplementary information (ESI) available. See DOI: https://doi.org/10.1039/d4ee02301c

is a significant process in biomass valorization as DFF holds high industrial potential in furan-based polyesters, pharmaceuticals, electrooptical devices, fungicides, *etc.* To date, Cd-based sulfides, $ZnIn_2S_4$, g-C_3N_4, halide perovskites and some composites have been developed for catalyzing the oxidation of HMF to DFF in acetonitrile (ACN).[5–9] However, this photocatalytic process is still at an early stage of development as there is a considerable lack of understanding and ongoing debate on the mechanisms governing the conversion of HMF into DFF in the liquid phase. Although certain photocatalytic systems have demonstrated commendable efficacy, and multiple putative reaction mechanisms involving charge transfer and radical interactions based on energy-level alignment have been postulated, the process remains yet to be elucidated owing to the mentioned condition-dependent reactivities of catalysts, as well as the obscure surface reaction in the organic phase.[10–13] This gap in knowledge hampers its further development and highlights the imperative for further investigation to elucidate the dehydrogenation of alcohols to aldehydes in the liquid phase including DFF synthesis from HMF.

Currently, the principle of catalyst design is well-understood and acknowledged as an essential approach to improve reaction efficiencies within the domain of photocatalysis.[14–16] As an indispensable part of heterogeneous photocatalysis, the reaction conditions of the catalyst also strongly affect the photosynthesis reaction and even exert a more substantial impact on the reaction kinetics, product selectivity and the overarching efficiency of the reaction. However, understanding the influence of solvents on the process of analogous light-induced reactions at the molecular level still faces significant challenges and uncertainties. Accordingly, there is still very limited knowledge on the solvent refinement to improve the photo-synthesis reaction efficiency. In most cases, researchers often conduct tests by simply replacing solvents to identify the optimal one, without delving deeper into the finer and more comprehensive regulation of solvents, thus confining exploration of their potential benefits. The changes in reaction rates and product distribution in different solvents are often attributed to the diversities of produced reactive oxygen species, differences in redox potential, polarities and dielectric constants of solvents.[17–21] In fact, solvents possess the ability to not only modify the surface chemistry by binding to active sites and (de)stabilizing surface intermediates but also to reduce reaction barriers, facilitate proton transfer, and even alter the reactivity of reactive oxygen species (ROS).[22–26] In other words, it is imperative to disclose the concomitantly critical effect of solvent dynamics, which frequently exert a significant impact on biomass conversion.

Based on these considerations, HMF oxidation into DFF was employed as a typical process, and we decided to take a different approach by optimizing the solvents to overcome the challenges associated with substantial enhancement in the efficiency, which has proven difficult through catalyst design alone. In our reaction system where $Cd_{0.75}Zn_{0.25}S$ nanoparticles were employed as the model catalyst and ACN (HPLC grade with water content <30 ppm) served as the solvent, it is observed that the reaction tended to stagnate after reaching a certain extent, despite the presence of a significant amount of unreacted HMF. Surprisingly, the addition of a small amount of water to the reaction system enabled continuous progression of the reaction, leading to a noticeable improvement in DFF yield. The product yield began to decline once beyond a certain proportion of water in the solvent. This intriguing and unique reaction phenomenon suggested that the role or mechanism of water or solvent in this reaction is far more complex than initially anticipated. Our results indicated that water molecules actively participated in the reaction process *via* the H-bonding interaction. Importantly, the same solvent refinement strategy was also applicable to other alcohol-to-aldehyde reactions and even other photocatalysts. This approach not only advances the photocatalytic reaction efficiency but also highlights the critical role of solvent grade in reducing energy consumption and promoting sustainable chemical processes.

Results

Photocatalytic HMF conversion into DFF and optimization

The characterization results of $Cd_{0.75}Zn_{0.25}S$ nanoparticles are given in the ESI† (Fig. S1–S3). The photocatalytic reaction was initially performed in air atmosphere at room temperature with ACN (HPLC grade, water content <30 ppm) as the solvent under blue LED irradiation. Fig. 1(a) indicates that the DFF yield reached 23.5% with about 40.5% HMF conversion after 12 h reaction in ACN, and FFCA (5-formylfuran-2-carboxylic acid, one of the over-oxidation products) was the main over-oxidation product with a yield around 3%. The mineralization amount of HMF was about 12% in ACN. However, DFF generation in ACN ceased after about 6 hours of reaction (Fig. 1(b)), and extending the reaction time cannot further improve the DFF yield; instead, the prolonged reaction time only resulted in increased HMF conversion. It is affirmed that the portion deviating from the carbon balance for HMF conversion almost entirely converted into inorganic carbon (called mineralization in later text), which was reflected by the gas chromatography–mass spectrometry (GC–MS) results of the reacted solution, as shown in Fig. S4 (ESI†). Furthermore, the DFF yield remained at a low level from 20% to 25% by changing the Cd/Zn ratio in $Cd_xZn_{1-x}S$ (Fig. S5, ESI†), but the conversion and mineralization percent of HMF both decreased with the increase in Cd content, indicating that the CB/VB position may have a significant influence on HMF conversion, while DFF formation may be mainly limited by other factors. Similarly, co-catalysts such as Au, Ag, Pt, Pd, Ru, Co, and Ni were unable to further increase the DFF yield in ACN due to the stagnant reaction process (Fig. S6a and Table S1, ESI†). We believe that these reaction phenomena also exist when using similar photocatalysts.

Interestingly, the addition of a small amount of water to the reaction solution can effectively overcome the issues of reaction stagnation and low product yield (original data are shown in Table S2, ESI†). As indicated in Fig. 1(c), starting from 0, the

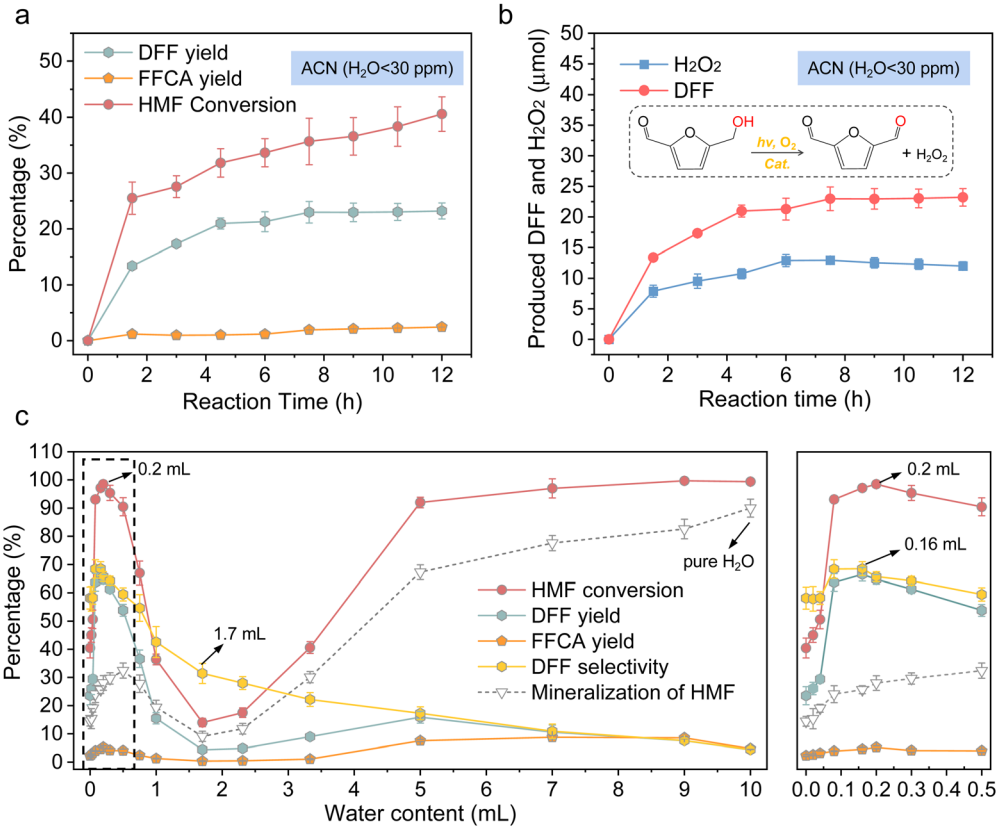

Fig. 1 (a) Time-dependent HMF conversion, DFF yield and FFCA yield in ACN over $Cd_{0.75}Zn_{0.25}S$. (b) Time-dependent DFF and H_2O_2 production in ACN over $Cd_{0.75}Zn_{0.25}S$. (c) HMF oxidation activity of $Cd_{0.75}Zn_{0.25}S$ in a mixed solution of ACN and H_2O (VH_2O + VACN = 10 mL; reaction time: 12 h).

gradual increase in the amount of water in the reaction system led to an increase in both the HMF conversion and the DFF yield, reaching their maximum values at a water content of 0.16 mL (VH_2O + VACN = 10 mL). The HMF conversion achieved an impressive 97%, while the DFF yield reached 66.6%. Subsequently, as the water content in the solvent further increased from 0.16 mL to 1.7 mL, both the HMF conversion and the DFF yield gradually declined. However, as the water content continued to increase, the HMF conversion started to rise again. Unfortunately, due to severe mineralization, the DFF yield remained consistently low. The fluctuating HMF conversion and DFF yield observed in this study indicate that water in the reaction system exhibited a more intricate influence and mechanism of action than initially anticipated. Control experiments (Fig. S7 and Table S3, ESI†) indicated that no DFF could be detected in the absence of catalyst, and the extra H_2O addition and O_2 are both essential for the high DFF yield. Under the atmosphere of N_2 and vacuum condition, there was almost no DFF product but with high HMF mineralization percent and small H_2 evolution after reaction, the O_2 atmosphere slightly restrained the activity of $Cd_{0.75}Zn_{0.25}S$. Additionally, the above-mentioned metal co-catalysts could further improve the DFF yield or selectivity to more than 80% only in the presence of trace water in ACN (Fig. S6b and Table S1, ESI†). Therefore, the focus of this study is to elucidate the reasons behind the reaction stagnation in the reaction system with acetonitrile as the solvent, as well as to understand the mechanism by which the introduction of water into the reaction solution led to the fluctuating HMF conversion and DFF yield.

First and foremost, the issue of sulfide experiencing photocorrosion under irradiation should be highlighted, resulting in decreased reactivity after the initial operation, irrespective of the addition of water, such deactivation often frequently occurs on bare sulfide photocatalysts and can be alleviated by other reported strategies (see regeneration procedures and Fig. S8 in ESI†).[10] Consequently, *in situ* surface-enhanced Raman spectroscopy (SERS) was initially employed to eliminate the ambiguous influence of surface changes of catalysts on our conclusions. The findings reveal the potential formation of an oxide layer on the surface, occurring regardless of the presence of additional water (as depicted in Fig. S8c and d, ESI†). This implies that analogous surface alterations occur irrespective of water addition, while the activity differs significantly. These observations refute the notion that variations in DFF yield and HMF conversion are attributed to the formation of a potentially active oxide layer caused by trace water in the solvent. The results strongly indicate that the fluctuations in faint water content do not modify the intrinsic nature of the catalyst, or to say, the physical properties of the catalyst changed in the same tendency; rather, they support the notion that performance disparities arise from the variation in the solvent composition.

Mechanistic study

To gain a deeper understanding of the chemical transformations occurring in the reaction system, the contents of the product and main byproducts were monitored. In line with previous studies, H_2O_2 was the main by-product in ACN (Fig. 1(b)). Nevertheless, the stoichiometric ratio between H_2O_2 and DFF in ACN was much lower than the theoretical value of 1 : 1 according to the previously proposed reaction path (see Fig. S9, ESI†), indicating the partial decomposition of produced H_2O_2.[12,27] What is more, the accumulated H_2O_2 concentration in ACN almost exhibited no decline during the reaction. Control experiment suggests that H_2O_2 alone cannot trigger HMF oxidation without catalyst under irradiation (Fig. S7b, ESI†). These results strongly implied that the formation and consumption of surface H_2O_2 on catalysts had reached a balanced state leading to the steady concentration of H_2O_2 in bulk ACN, and thus may block the active sites by preferentially reacting with active species due to the relatively strong affinity of the O–O bond in H_2O_2 with metal sites, and then leading to the cessation of DFF generation. This speculation was supported by DFT calculation results, H_2O_2 and HMF are both energetically favorable to be absorbed on the Zn sites of bare $Cd_{0.75}Zn_{0.25}S$ (Fig. S10, ESI†), and the H_2O_2 absorption is more favorable than HMF (−1.19 eV of H_2O_2 *vs.* −0.8 eV of HMF). Such detrimental effect of H_2O_2 was further experimentally demonstrated by the photocurrent response and pre-adding a small amount of oxalic acid (10 mg) in ACN during the reaction, as the current density of $Cd_{0.75}Zn_{0.25}S$ (Fig. S11a, ESI†) was greatly restrained in the presence of H_2O_2, and a relatively high DFF yield (60%) was obtained (Fig. S11b, ESI†) owing to the accelerated H_2O_2 decomposition ($H_2C_2O_4 + H_2O_2 \rightarrow CO_2 + 2H_2O$) by oxalic acid.

In contrast, no H_2O_2 was detected in the presence of 160 μL H_2O after 12 hours of reaction. To clarify whether H_2O_2 was produced or not during the reaction, the time-dependent H_2O_2 concentration was determined. It was found that the accumulated H_2O_2 increased first and then decreased within all mixed solutions, and its variation tendencies were closely related with the H_2O contents in ACN (Fig. S11c and d, ESI†), in accordance with the activity. The produced H_2O_2 had been completely decomposed in the presence of 160 μL H_2O, and the highest apparent H_2O_2 decomposition rate (Fig. S11e, ESI†) was observed under the optimal condition of 160 μL H_2O addition. In addition, the DFF yield and HMF conversion could still be maintained to be more than 63% and 90% respectively with nearly no H_2O_2 production in the presence of 160 μL H_2O even though the initial HMF concentration was increased to 50 mM (Fig. S12a, ESI†); this result indicated the state-of-the-art performance in the current study with an average DFF productivity of about 27.3 μmol h^{-1} (see Table S4, ESI†). By comparison, the evolved H_2O_2 and DFF were almost linearly increasing with the increase in substrate concentration without water addition (Fig. S12b, ESI†), whereas the DFF yield and HMF conversion decreased, also implying that H_2O_2 was indeed produced by the hydroxymethyl dehydrogenation instead of two-electron water oxidation of the trace amount of H_2O in ACN. Moreover, HMF conversion and DFF formation rate were both inhibited once 160 μL H_2O containing H_2O_2 was pre-added into ACN (Fig. S12c and d, ESI†), indicating again that H_2O_2 is unfavorable to the reaction process, which was further supported by the subsequent *in situ* electron spin resonance (ESR) spectrum.

Although the introduction of water ensured the continuous progress of the catalytic reaction, the yield of DFF was also influenced by the reaction selectivity or, in other words, HMF mineralization. Therefore, before further investigating the mechanism of water's role, it is necessary to understand the types of reactive oxygen species and their roles in the reaction process. To investigate this, *in situ* ESR and trapping experiment were performed. The results evidenced that three active oxygen of $^{\bullet}O_2^-$, $^{\bullet}OOH$ (protonated $^{\bullet}O_2^-$) and $^1O_2$ existed (Fig. S13, ESI†), and no signal of $^{\bullet}OH$ was detected in both ACN and the mixed solution with 160 μL H_2O.[28,29] The trapping experiment (Fig. S14, ESI†) indicated that both $^{\bullet}O_2^-$ and $^1O_2$ were the key active ROS during the reaction. Nevertheless, it was $^{\bullet}O_2^-$ that led to persistent mineralization of HMF on account of nearly no mineralization after $^{\bullet}O_2^-$ was trapped, and the mineralization of HMF still reached a high level close to the control after $^1O_2$ was trapped. Moreover, a pretty low DFF yield was obtained once $^1O_2$ was quenched, indicating that $^1O_2$ was the practical active oxygen that was directly responsible for DFF formation.

With the increase in the amount of introduced water, its impact on the reaction was divided into three stages. The first stage occurred between 0 and 0.16 mL or 0.2 mL, where both the HMF conversion and DFF yield increased with the water content. The second stage took place between 0.2 and 1.7 mL, where both the HMF conversion and DFF yield decreased as the water content increased. The third stage spanned from 1.7 to 10 mL, where the HMF conversion increased with the water content, but the DFF yield did not show any significant increase. In order to conduct an in-depth investigation into the role of water in different stages, we first conducted a study on the form of water and HMF, and their interactions in the solution by Raman spectrum and molecular dynamics (MD) simulation. The spectrum (Fig. 2(a)–(c)) of the mixed solution with different H_2O/ACN ratios indicated that H_2O existed as a single molecule when the H_2O concentration was low (<17 vol%), while the intermolecular hydrogen bond would be formed once the H_2O content was further increased. This result was in good agreement with the molecular dynamics (MD) simulation (the overall and localized solvation structures of HMF in different solvents are given in Fig. S15, ESI†), no hydrogen bonds were observed in the system with 160 μL H_2O and 10 mM HMF equivalent, and the average number of hydrogen bonds in the system increased to 3.3 when the water content was increased to 1.7 mL equivalent. The average number of H-bonding further increased to 33.9 in pure water (Table S5, ESI†). These results implied that H_2O and HMF molecules are both isolated in bulk solvent when the water content is low, while H-bonding interaction occurs with the increased water addition. The radial distribution functions (RDFs; Fig. 2(d)) of oxygen atoms around the hydroxyl-H atom

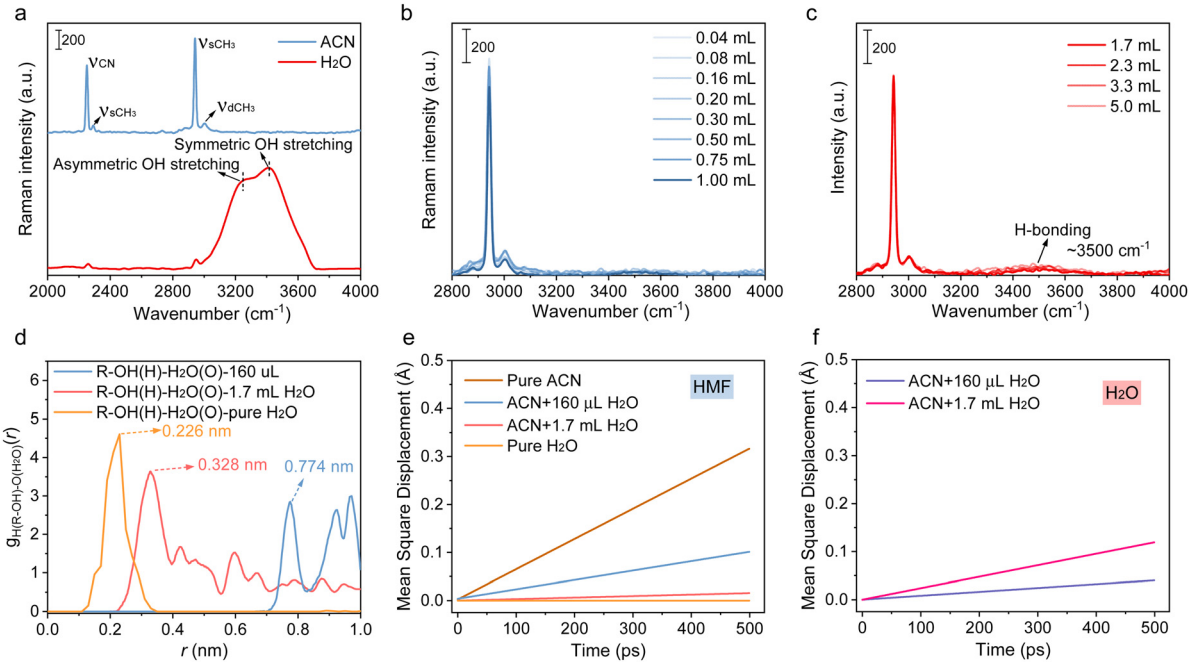

Fig. 2 (a) Raman spectrum of ACN and water. (b) and (c) Raman spectrum of ACN with different H_2O contents (water content: 0 to 50 vol%). The strong hydrogen interaction generates the asymmetric stretching vibration of OH, whereas weak hydrogen bonds cause the symmetric stretching vibration of OH. The result demonstrates that when water content is low, the hydrogen bonds between the water molecules are totally disrupted and the water molecule remains in the solution as a single molecule. (d) Radial distribution functions of oxygen atoms around the hydroxyl hydrogen of hydroxymethyl. (e) and (f) MSD curves of HMF and H_2O in different solvent compositions.

in hydroxymethyl indicate that there is a long distance (0.774 nm) between the H atom and the O atom of H_2O, further revealing that the H-bonding interaction is nonexistent between HMF and H_2O, while a peak at 0.328 nm attributed to H-bonding can be observed in the first coordination shell of the hydroxyl-H atom with the surrounding H_2O molecule in the presence of 1.7 mL H_2O equivalent. The peak of the first coordination shell of the hydroxyl-H atom further decreased to 0.226 nm in pure water, implying that the hydrogen bonding interaction between HMF and H_2O gradually strengthens as the water content increases.

Since H_2O can alter the amount of hydrogen bonds or the polarizability of reactants, both of which can stabilize the transition state of the reaction intermediate, H_2O often plays a more substantial role when there is a variation in the dipole orientation between the reactant and the transition state.[30] For instance, the polar effect of H_2O can stabilize the accumulated negative charge on oxygen (shown in Fig. S16, ESI†), increasing the dipole moment of $^{\bullet}OH$, $^{\bullet}O_2^-$ and $^{\bullet}OOH$. In this case, their reactivities were much higher than that in bare ACN owing to developed dipole moments.[31] As demonstrated by previous kinetic studies, the hydrogen abstraction rate constants of $^{\bullet}OH$ from organic substrates in aqueous solutions are often one to two orders of magnitude higher than that in ACN.[32] These discussions give reason to why the mineralization of HMF becomes the overwhelming process in the mixed solvents with high water contents (>17 vol%) or in pure H_2O, because water can act as a H-bond acceptor or donor to bond either with the hydroxyl group in HMF or with the ROS in solvent *via* weak interactions. On the one hand, the HMF molecules could be solvated due to hydrogen bonding with solvent molecules, making it difficult to be adsorbed on the catalyst surface. On the other hand, the hydrogen bond interaction not only enhanced the reactivity of $^{\bullet}O_2^-$, but also even converted it into $^{\bullet}OH$ ($^{\bullet}O_2^- + H^+ \rightarrow {}^*O + {}^{\bullet}OH$) in the presence of massive water. As indicated in Fig. S17a (ESI†), only $^{\bullet}OH$ can be detected in pure water. These species then reacted with solvated HMF non-selectively in the bulk solvent, resulting in its deep mineralization. Similar conclusions can also be extended to other solvents with a relatively strong hydrogen bonding capacity, such as DMSO and DMF, in which the product yield was much lower than that in ACN but displayed a high conversion and mineralization of HMF (Fig. S17b, ESI†). Therefore, controlling the water content at a lower level (<17%) can effectively reduce the mineralization of HMF. However, based on the reaction data, when the water content exceeded 0.2 mL, the excessive isolated water molecules near the surface of the catalyst may exhibit a strong competitive adsorption effect on HMF. This resulted in a deterioration of the reaction, as observed in the range from 0.2 mL to 1.7 mL in Fig. 1(c), where both the DFF yield and HMF conversion decreased with the increase in water content.

The above discussion can also be supported by further DFT and MD simulations of the different solvent compositions contenting 10 mM HMF equivalent. H_2O was energetically favorable with a moderate absorption energy of −0.58 eV on the catalyst (Fig. S18, ESI†). Thus, the presence of excess

isolated water was detrimental to the adsorption of HMF, as it engaged in competitive adsorption for the active sites on the catalyst's surface. What is more, as suggested by the mean square displacement (MSD) of HMF and H_2O in Fig. 2(e), the diffusion rate of HMF from bulk solvent to catalyst surface decreased with the increase in water content, attributed to strengthened H-bonding interaction with H_2O, which stabilizes HMF in bulk solvents, as indicated by the decreased H-bond length in RDFs. In pure water, HMF is totally solvated, its diffusion can hardly occur, and it is difficult to approach the catalyst surface. Moreover, the diffusion of H_2O is easier than that of HMF in the mixed solvent (Fig. 2(f)), indicating that the excessive water may form a covering layer that impeded the access of HMF to the surface of the catalyst. In this case, the oxidation of the alcohol group is typically unfavorable, thus leading to reduced HMF conversion and DFF yield ranging from 0.2 mL to 1.7 mL H_2O addition. The above-mentioned experiments and simulations together elucidate the experimental results, in which massive isolated water is unfavorable for the efficient oxidation of hydroxymethyl groups, whereas HMF is stabilized in the bulk solvent phase and then mineralized by free radicals once large amounts of water are present.

Besides, these analyses are proved by the experimental results obtained after adding 160 μL D_2O instead of H_2O. As displayed in Fig. 3(a)–(c), the enhancement of H-bonding interaction by introducing D_2O slightly facilitated HMF conversion but imposed no enhancement on DFF formation. Accordingly, a secondary kinetic isotope effect (KIE) was observed for both HMF conversion and DFF formation, indicating that water molecules affect the DFF formation and HMF conversion *via* hydrogen bonding with other surface species. It was also found that the mineralization of HMF was dramatically accelerated in the presence of D_2O (Fig. 3(c)), which displayed a solvent isotope effect (SIE) compared with that containing H_2O, giving further evidences that the H-bonding interaction between the reactants and oxygen-containing radicals in the bulk phase of solvent only led to the deterioration of HMF mineralization.[33] To gain more insights into the surface reaction, 5,5-dimethyl-1-pyrroline-*N*-oxide (DMPO) was added as a radical scavenger (Fig. S19, ESI†), and it can be seen that the HMF conversion and DFF formation were completely suppressed, verifying that HMF conversion proceeds *via* a radical intermediate pathway.[34] The carbon-central radical (R-$^{\bullet}$CH(OH)) was affirmed as the intermediate from the C–H bond cleavage of hydroxymethyl (Fig. 3(d)), as the carbon-central scavengers of butylated hydroxytoluene (BHT) greatly suppressed DFF formation (Fig. S19, ESI†). The addition hole scavenger of triethanolamine (TEOA) almost completely blocked HMF conversion (Fig. S19, ESI†), implying that photoinduced holes are indispensable for DFF formation, which is further revealed by *in situ* ESR. In Fig. 3(e), no attenuation of the DMPO-R-$^{\bullet}$CH(OH) signal was observed once $^{\bullet}O_2^-$ and $^1O_2$ were quenched, while the signal intensity of DMPO-R-$^{\bullet}$CH(OH) sharply decreased in the presence of hole scavengers, suggesting that R-$^{\bullet}$CH(OH) was not produced by the interaction between the C–H bond in hydroxymethyl and $^{\bullet}O_2^-$ or $^1O_2$ but the direct attacking by photogenerated holes.

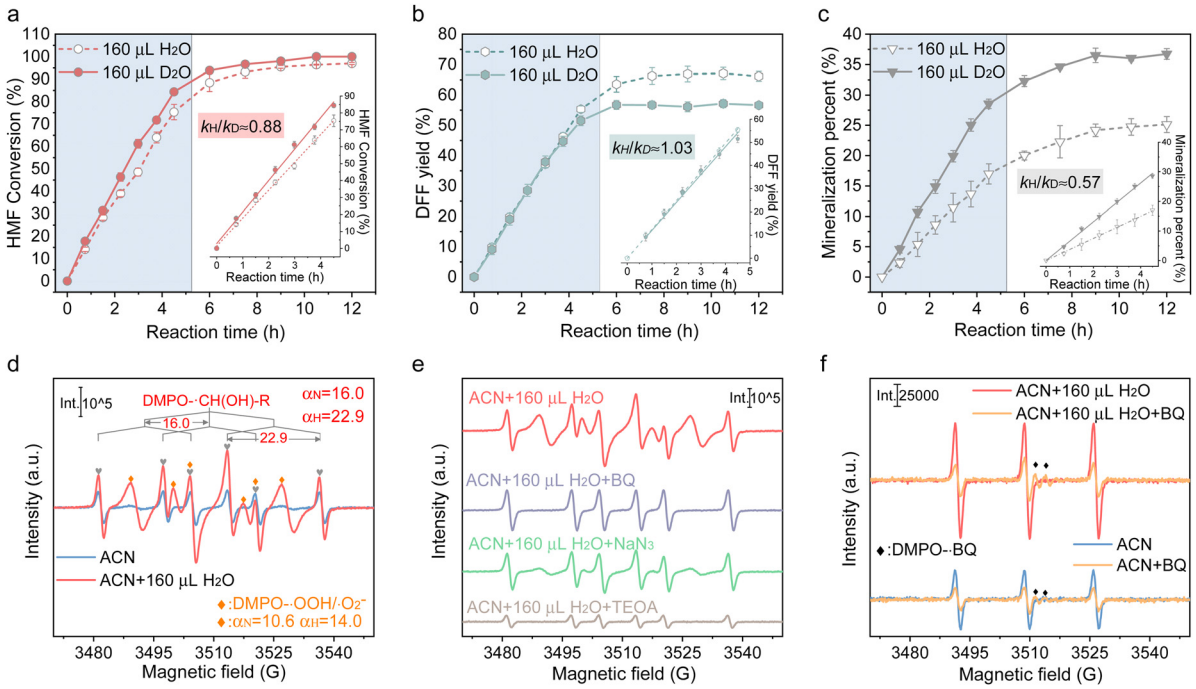

Fig. 3 Time-dependent efficiency of HMF oxidation over $Cd_{0.75}Zn_{0.25}S$ in H_2O/ACN and D_2O/ACN: (a) conversion of HMF; (b) yield of DFF; and (c) mineralization percent of HMF. Kinetic isotope effect (KIE): 0.88 for HMF conversion, 1.03 for DFF production, and 0.57 for mineralization. (d) and (e) *in situ* ESR signal of DMPO-R-CH(OH) over $Cd_{0.75}Zn_{0.25}S$ after 20 min irradiation under different conditions (In ACN, ACN + H_2O, ACN + H_2O + BQ, ACN + H_2O + NaN_3, ACN + H_2O + TEOA). (f) *In situ* ESR signal of TEMPO-$^1O_2$ over $Cd_{0.75}Zn_{0.25}S$ in ACN and ACN + H_2O with or without adding $^{\bullet}O_2^-$ quencher (the original ESR spectrum is given in Fig. S13, S22 and S23, ESI†).

The result also showed that $^1O_2$ was mainly produced by the electron transfer between $^\bullet O_2^-$ and holes ($^\bullet O_2^- + h^+ \rightarrow {}^1O_2$), because the $^1O_2$ signal in both ACN and ACN + H_2O decreased significantly once *p*-benzoquinone (BQ, $^\bullet O_2^-$ trapper) was added (Fig. 3(f)). What is more, the relative intensity of $^1O_2$ linearly increased with the intensity of $^\bullet O_2^-$ (Fig. 4(a)). It has been indicated that if the $^1O_2$ were produced by the bi-molecular dimerization reaction of $^\bullet O_2^-$ and $^\bullet$OOH ($2{}^\bullet O_2^- + 2H^+ \rightarrow {}^1O_2 + H_2O_2$, $2{}^\bullet OOH \rightarrow {}^1O_2 + H_2O_2$), its signal would be much more intensive under higher $^\bullet O_2^-$ concentration.[35,36] As given in Fig. 4(b) and (c), the appropriate quantity of water addition also greatly enhanced the signals of $^\bullet O_2^-$/$^\bullet$OOH, $^1O_2$, and R-$^\bullet$CH(OH), where their signals monotonically increased with the prolonged reaction time, rather than almost tended to be invariable after certain time irradiation in ACN due to the adverse effects caused by H_2O_2. It is worth noting that the relative amount of $^\bullet O_2^-$/$^\bullet$OOH in ACN increased first and then decreased, attributed to the quick consumption of $^\bullet O_2^-$/$^\bullet$OOH during irradiation (Fig. 4(d)).

It is (Fig. S20, ESI†) indicated that the activation barrier for H_2O_2 decomposition by holes over the bare catalyst surface is as high as 183.7 kJ mol^{-1}, whereas the activation barrier was relatively low (114.6 kJ mol^{-1}) to produce surface *OH *via* the electron induced pathway. The presence of water can largely lower the activation barriers of the electron-induced pathway for H_2O_2 decomposition to only 6.6 kJ mol^{-1} *via* H-bonding interaction, thus facilitating H_2O_2 removal. However, the H_2O_2 decomposition by holes was still as high as 129.7 kJ mol^{-1} even with H-bonding interaction, and thus H_2O_2 decomposition by holes was kinetically unfavorable. We therefore inferred that H_2O_2 decomposition mainly undergoes an electron-induced pathway ($H_2O_2 + e^- \rightarrow {}^*OH + OH^-$) in the presence of water, instead of the hole-induced pathway ($H_2O_2 + h^+ \rightarrow H^+ + {}^*OOH$). Moreover, the absorption energy of O_2 on the Zn site of $Cd_{0.75}Zn_{0.25}S$ (−1.14 eV; Fig. S21, ESI†) was proved to be quite close to that of H_2O_2 (−1.19 eV), thus the residual H_2O_2 in ACN also adversely affected oxygen activation, and as illustrated by the ESR results in Fig. 4(e) and (f), the signals of $^\bullet O_2^-$ and $^1O_2$ both decreased with the increase in H_2O_2 concentration once water containing equivalent H_2O_2 was pre-added into ACN before radiation. Overall, the occurrence of H_2O_2 is unfavorable for the normal progression of the reaction process as it blocks the active sites of HMF activation and also exhibits a negative impact on the O_2 activation. Thus, a reasonable explanation for the suppressed activity under an O_2 atmosphere is that the excessive O_2 may restrain the electron-induced pathway of H_2O_2 decomposition by the competitive process of electron trapping for $^\bullet O_2^-$ generation.

In situ ATR-SEIRAS and isotope labeling were carried out for further clarifying the key role of water and O_2 during the DFF formation process. The *in situ* ATR-SEIRAS in ACN without H_2O addition is shown in Fig. 5(a), and the peak located around at 1109 cm^{-1} corresponded to the $\nu_{(C-O)}$ mode of bidentate bridged *CH_2OH of the hydroxymethyl group in HMF.[37–39] The peaks over 1363 cm^{-1} and 1443 cm^{-1} can be attributed to the deformation and symmetric stretching vibration of the C–H bond in the CH_2OH group, which were further proved by the typical absorption bands located at 2867 cm^{-1},

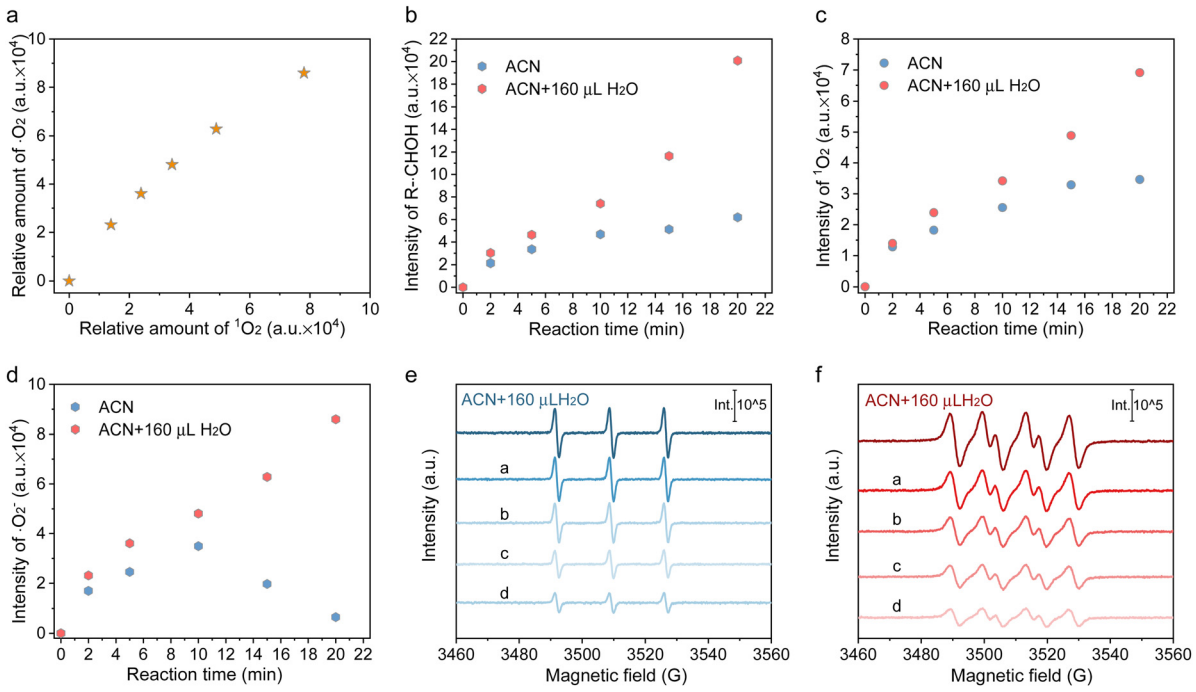

Fig. 4 (a) Relative amount correlation between $^\bullet O^{2-}$ and $^1O_2$ in ACN + H_2O (the original data are given in Fig. S13, ESI†). (b)–(d) Time-dependent *in situ* ESR signal intensity of R-CH(OH), $^\bullet O_2^-$ and $^1O_2$ over $Cd_{0.75}Zn_{0.25}S$ during 20 min irradiation (the original results are given in Fig. S13, ESI†). (e) and (f) ESR signals of $^1O_2$ and $^\bullet O_2^-$/$^\bullet$OOH in ACN + 160 μL H_2O with pre-adding a certain amount of H_2O_2 after 20 min irradiation (a: 0.5 equiv.; b: 1 equiv.; c: 2 equiv;. d: 4 equiv.; the original spectrum is given in Fig. S24 and Fig. S25, ESI†).

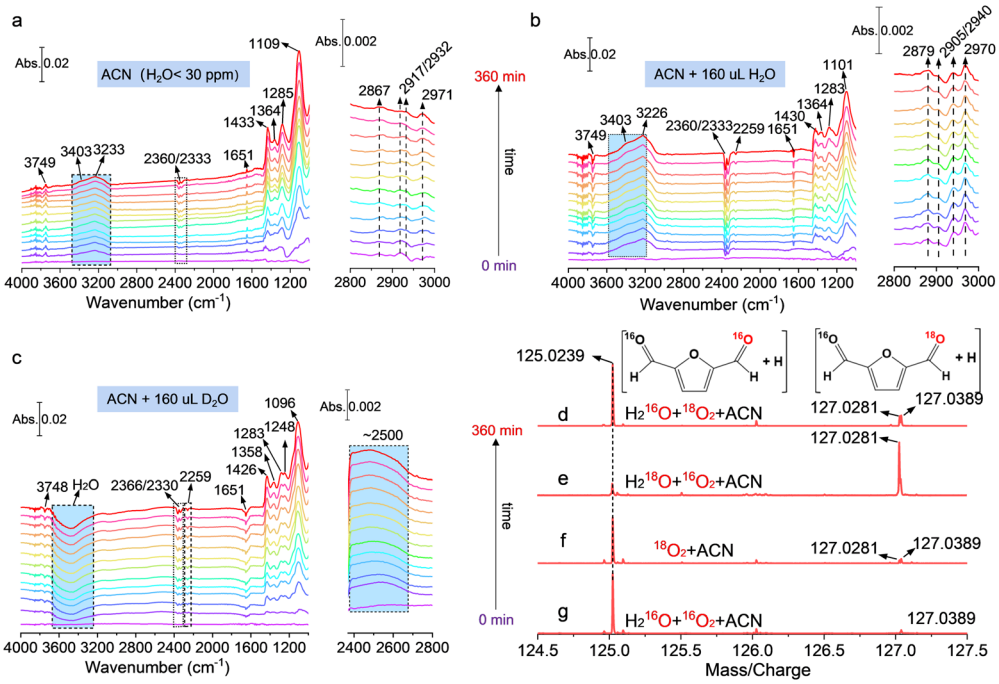

Fig. 5 *In situ* ATR-SEIRAS measurement of HMF selective to DFF over $Cd_{0.75}Zn_{0.25}S$ in different reaction mediums: (a) ACN; (b) ACN + H_2O; and (c) ACN + D_2O. (d)–(g) High-resolution mass spectrum of the products using different isotopes.

2917/2932 cm^{-1} and 2971 cm^{-1} of the C–H bond.[37] It can be concluded that HMF was anchored on the catalyst surface in the form of bidentate adsorption through C–H and C–O of the hydroxymethyl group. The downward peaks at 2360/2333 cm^{-1} are ascribed to the interface CO_2 derived from the partial mineralization of HMF, and the band at 2259 cm^{-1} and 1285 cm^{-1} corresponded to the cyano group of interfacial ACN and over-oxidation product of HMF, respectively. No typical C=O bond located at ~1700 cm^{-1} is observed, which suggested that the aldehyde group can hardly be absorbed on the surface of the catalyst, explaining the low yield of carboxyl-containing products such as FFCA and FDCA under current conditions.

The band located at 1651 cm^{-1} was assigned to the O–H bending vibration mode (δ_{O-H}), and the broad absorption bands from about 3100 cm^{-1} to 3800 cm^{-1} corresponded to the O–H stretching vibration mode (ν_{O-H}). The incremental frequency of ν_{O-H} originated from the decreased degree of hydrogen bonds on the catalyst, which led to the increased mobility of surface O–H. Specifically, the bands located near 3749, 3403, and 3233 cm^{-1} were attributed to the surface hydroxy, isolated water molecule, and H-bonded water.[40,41] The increased vibration intensity of water at 3403 cm^{-1} and 3233 cm^{-1} with irradiation time suggested that H_2O was actually one of the products from the dehydrogenation of hydroxymethyl, and this result is totally different from the previous report that H_2O_2 was generated as the only by-product from proton transfer. Moreover, the upward peaks of surface hydroxy at 3749 cm^{-1} in Fig. 5(a) more probably originated mainly from the dissociation of surface water, because the peak of surface hydroxy became downward and its vibration intensity increased with irradiation time after adding 160 μL H_2O in ACN (Fig. 5(b)), corresponding to the ongoing lessening of surface hydroxy. Such observation indicated that water also participated in the dehydrogenation of hydroxymethyl as a reactant. This conclusion is supported by the results after replacing H_2O with D_2O (Fig. 5(c)), where the peaks of surface hydroxy, isolated water, and H-bonded water became downward, and a distinct upward vibration peak assigned to D–O bond stretching was observed at 2500 cm^{-1}, giving direct evidence that D–O was generated due to D_2O dissociation on the surface of the catalyst.[12] Accordingly, the absorbed surface hydroxy could act as a proton-acceptor to form H_2O with the proton from $-CH_2OH$. However, electron-induced H_2O_2 dissociation into surface hydroxy can still not be excluded.

The high-resolution time-of-flight mass spectrum (TOF-MS) in Fig. 5(d)–(g) shows the results using labeled water ($H_2{}^{18}O$) and oxygen ($^{18}O_2$), which further clarify the role of H_2O and O_2. The peaks located at a mass/charge ratio of 125.0239 correspond to DFF with no ^{18}O incorporation, whereas the peak at 127.0281 belongs to the DFF with one ^{18}O atom incorporation. As indicated in Fig. 5(e), the strong peak corresponding to one ^{18}O atom incorporation into DFF was observed when $H_2{}^{18}O$ was used under an $^{16}O_2$ atmosphere, as a result of rapid hydroxy exchange between surface CH_2OH^* with ^{18}OH from $H_2{}^{18}O$ dissociation.[30,42] The result here implied that there was almost no O–O bond cleavage during the reaction and the O_2 play only as the proton-acceptor to form surface OOH species during hydroxymethyl dehydrogenation, which is in good agreement with the *in situ* ESR result that activated oxygen do not drive for

C–H cleavage. As contrast, two very weak peaks of ^{18}O incorporation were detected under $^{18}O_2$ atmosphere when using ACN and ACN + $H_2{}^{16}O$ as the solvent (Fig. 5(e) and (f)). A possible reason for this was that the produced surface $H_2{}^{18}O_2$ undergoes dissociation into two $^{18}OH^*$, which then participated in the surface reaction and as the proton acceptor to form $H_2{}^{18}O$, leading to minor ^{18}O incorporation.

It should also be noted that the identical IR absorption peak assignment and similar peak positions with or without water addition (Fig. 5(a) and (b)) implied the same reaction intermediates and identical intrinsic pathway of DFF formation in ACN or a mixed solution of ACN and water, which also demonstrated that the addition of water did not change the reaction pathway of DFF evolution, and the trace amount of water in ACN itself (<30 ppm) contributed a lot to HMF photocatalytic oxidation. Moreover, the much stronger peak intensity of H-bonded water in Fig. 5(a) and (b) also verified that the surface water was mainly hydrogen-bonded with each other or surface species such as $–CH_2OH$, considering that the vibration frequency of $*CH_2OH$ slightly decreased with the enhanced H-bond degree of solutions (ACN < H_2O + ACN < D_2O + ACN).[33,43] In light of the above-mentioned findings, a control experiment using anhydrous ACN (H_2O < 10 ppm, absolute anhydrous ACN cannot be obtained) was performed (Fig. S26, ESI†), and the result showed that the HMF conversion and DFF yield are almost the same as that in ACN with 30 ppm H_2O, but a higher H_2O_2 concentration (~25% higher than that in HPLC-grade ACN) was observed. Even though about 40% H_2O_2 was still decomposed during the reaction in anhydrous ACN, giving rise to about 16 ppm H_2O remained in the reaction medium, which was even higher than the water contained in anhydrous ACN itself. We therefore deduced that the H_2O in the solvent itself and that originating from H_2O_2 decomposition both play a decisive role in the reaction process. Combining with the observed secondary KIE effect, it can be inferred that water had been involved in the dehydrogenation of hydroxymethyl process by promoting bond activation in hydroxymethyl and H_2O_2 removal *via* the surface hydrogen bond interaction. It should also be acknowledged that truly anhydrous polar solvents are typically nonexistent; that is to say, our work here indicates that the selection of solvent grade plays a crucial role in the outcomes of similar reactions and may even lead to misjudgments of the conclusions.

The DFT calculation provided further insights into the water-involved reaction process. As given in Fig. S27 (ESI†), the adsorption of HMF on CZS (002) was more energetically favorable with the help of moderate isolated water, which increased the adsorption energy from −0.8 eV to −1.38 eV, suggesting that surface water could facilitate HMF adsorption by H-bonding interaction with the O–H bond. Charge distribution analysis near surface showed a clear electron depletion region around the metal-O bond, whether water existed or not (Fig. S28, ESI†), demonstrating a hole-dependent bond cleavage path combining with the difference charge density of bare $Cd_{0.75}Zn_{0.25}S$, in line with our experimental results. The kinetic results (Fig. 6(a)) evidenced that the initial activation of hydroxymethyl can hardly occur on the bare catalyst surface. Specifically, the activation barriers for the dissociation of HMF *via* $–CH_2OH$ over CZS (002) without water are as high as 278.4 and 150.6 kJ mol^{-1} for C–H (Fig. S29a, ESI†) and O–H (Fig. S29b, ESI†) bonds, and thus, the bond cleavage by catalyst alone was unlikely. The presence of surface-bound water intermediates, however, can facilitate bond activation *via* H-bonding in much the same way as it occurred in the bare catalyst surface without H-bonding. This process lowered the barrier for the activation of the C–H bond by 108.9 kJ mol^{-1} (Fig. S29c, ESI†). The presence of adsorbed water intermediates also lowered the subsequent activation barrier of O–H to 88.1 kJ mol^{-1} (Fig. S29d, ESI†) for the ensuing carbon-central intermediate to form the aldehyde over the surface of the catalyst. The ability of adsorbed water to effectively activate both the O–H and C–H bonds helped to explain the overall increase in catalytic activity in the presence of trace amounts of water in the solvent. Note that the reaction path shown in Fig. 6(b) is nonexistent according to the *in situ* ATR-SEIRS results and the high C–H bond activation energy on the bare catalyst. Therefore, as shown in Fig. 6(c) and (d), this reaction will begin with $^1O_2$ formation and H_2O dissociation, generating surface hydroxy (energy barrier: 73.9 kJ mol^{-1}; Fig. S30a, ESI†). The $^1O_2$ and surface hydroxy could accept the protons originating from hole-driven C–H and O–H bond cleavage, respectively, to form *OOH species (53.0 kJ mol^{-1}; Fig. S30b, ESI†) and regenerate surface H_2O with nearly no energy barriers (3.8 kJ mol^{-1}; Fig. S30c, ESI†). Then, the *OOH species can easily (23.7 kJ mol^{-1}; Fig. S30d, ESI†) extract proton from adjacent H_2O to form H_2O_2 and surface hydroxy, and thus, close the catalytic cycle. The overall reaction pathways are also shown in Fig. S31 (ESI†) step by step, where the first three steps refer to H_2O dissociation and $^1O_2$ formation, the fourth and fifth steps represent the dehydrogenation of the hydroxymethyl to form DFF, the sixth step is water regeneration, and the last two steps are H_2O_2 generation. Thereafter, the formed H_2O_2 would then decompose with nearly no energy barrier (6.6 kJ mol^{-1}, *vs.* 114.6 kJ mol^{-1} without water) *via* H-bonding interaction (Fig. S32, ESI†). Overall, the water-involved pathway greatly reduced the energy barriers of C–H, O–H and H_2O_2 decomposition but hardly increased the proton migration barrier (Fig. S33, ESI†), and the energy barriers of *OOH and H_2O_2 formation in the presence of water increased by less than 10 kJ mol^{-1}.

Broadening applications of water-addition strategy to other alcohol oxidation reactions and catalysts

In light of the above, 14 kinds of different substrates containing hydroxyl groups were investigated under the same conditions (Table S7, ESI†). The results indicate that water-promoted alcohol oxidation in ACN could be further effectively extended to other aromatic and heterocyclic alcohols. The corresponding aldehyde yields of phenethyl alcohol, furfuryl alcohol, thenyl alcohol and pyridinemethanol, as well as benzyl alcohol and its various *para*-orientating derivatives, can be further improved by adding a trace amount of water into the reaction medium. For example, the yield is improved from 48.7% to 80.6% for

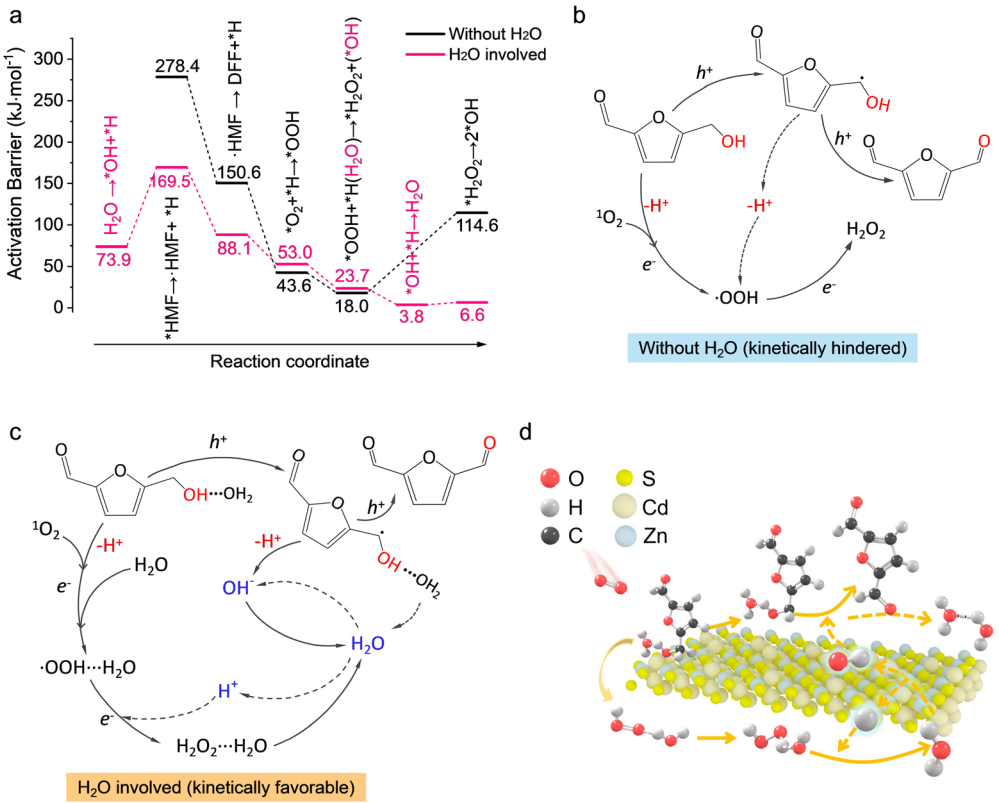

Fig. 6 (a) Activation barriers of the elementary reaction during HMF dehydrogenation in the absence (dark line) and presence (pink line) of water. (b) Schematic of the dehydrogenation pathway without water participation. (c) and (d) Schematic of the water-involved reaction pathway of HMF dehydrogenation to DFF.

benzaldehyde, 17.9% to 48% for furfural, and 26.2% to 53.4% for acetophenone, *etc.* Additionally, although the yields of Cyclohexanecarboxaldehyde (6.5%) and Cyclohexanone (8.8%) are relatively low even after adding water to ACN, they are still much higher than that in ACN alone.

Sulfides and g-C_3N_4 are two kinds of most widely reported catalysts for HMF conversion for their visible light harvesting ability, thus we employed them for the conceptional proof of the proposed tactic in this work, including CdS, Mn-doped CdS ($Mn_{0.2}Cd_{0.8}S$), $CdIn_2S_4$, $ZnIn_2S_4$, and carbon-doped g-C_3N_4 (C-g-C_3N_4; pristine g-C_3N_4 has no DFF for its high-valence potential). Upon optimization, the results shown in Fig. S34 (ESI†) indicate a substantial enhancement in DFF yield for various photocatalysts: from 18.1% to 65.8% for CdS, from 12.2% to 35.9% for $Mn_{0.2}Cd_{0.8}S$, from 7.2% to 18.7% for $CdIn_2S_4$, and from 10.2% to 17.5% for C-g-C_3N_4, achieved solely by adding a small amount of water to ACN. However, the optimal water contents vary for different catalysts, possibly owing to their distinct structural nature. For CdS and $Mn_{0.2}Cd_{0.8}S$, the optimal water content remains at 160 μL. Conversely, for $CdIn_2S_4$, the optimal water content is 200 μL, while for C-g-C_3N_4, it decreases to 120 μL. Notably, fresh $ZnIn_2S_4$ exhibits high DFF selectivity (nearly 85%) and HMF conversion (over 80%) at a low initial HMF concentration (10 mM) in ACN, but as the HMF concentration increases, both the HMF conversion and the DFF yield decrease without water addition (50.3% HMF conversion and 28.8% DFF yield at 50 mM; Fig. S35a, ESI†). With the addition of 300 μL water in ACN, the HMF conversion and DFF yield over $ZnIn_2S_4$ remain at a high level of approximately 65% even if the initial HMF concentration increases to 50 mM (Fig S35b, ESI†), aligning well with the observed phenomenon in $Cd_{0.75}Zn_{0.25}S$.

However, it is noteworthy first that the solvent-mediated strategy proposed in this work for enhancing the activity of the reaction system should at least be based on one of the following two assumptions: (1) the catalyst demonstrates certain activity for the catalytic conversion of HMF in ACN; or (2) the catalyst has a low tolerance for H_2O_2. Moreover, the choices for photocatalysts capable of efficient aerobic oxidization of HMF are currently quite limited. Apart from the mentioned materials, other available catalysts reported in the literature are either based on these materials and overly complex to prepare or exhibit major deficiencies (mainly refers to broad-band gap, over high-valence potential, *etc.*) and not suitable for this conversion. Overall, it has been proved that the observed water-promoted efficiency extends beyond the analogous aerobic photocatalytic dehydrogenation of hydroxyl groups to corresponding aldehydes, and is applicable to a range of other catalysts. Nevertheless, there remain numerous materials that we are not able to verify individually in this work due to the cognitive limits of photocatalytic HMF conversion at current stage, which need further study.

Conclusions

In summary, the study starts from a very interesting phenomenon, *i.e.* the spontaneous termination reaction of HMF to DFF over $Cd_{0.75}Zn_{0.25}S$ in ACN, while the HMF conversion was only 40.5%, with only 23.5% DFF yield. H_2O_2 was the main by-product as a result of hydroxymethyl dehydrogenation, which is unfavorable to the reaction. Miraculously, adding trace amounts of water into the reaction could effectively reverse the unfavorable circumstances of the reaction. The yield of DFF can reach about 66.6% with more than 97% HMF conversion. This optimization reduces energy losses associated with by-product formation, leading to a more efficient reaction pathway. It was found that both O_2 and water were indispensable for efficient DFF production. The addition of water not only promoted H_2O_2 decomposition, but also facilitated hole-derived C–H and O–H bond activation of HMF *via* intermolecular H-bonding. Importantly, the extra water did not change the reaction path of DFF production, and the trace water contained in ACN itself (<30 ppm) had been directly involved in the dehydrogenation of hydroxymethyl and played a key role even without adding extra water. Our findings on the positive impacts of water could be applied to other photocatalytic processes, offering pathways to enhance the energy efficiency and sustainability in a wide range of applications, contributing to the further development of efficient and sustainable fine chemical production system.

Methods

Materials

All the reagents were purchased and used without further purification. Self-made ultrapure water with an electrical resistivity of 18 MΩ cm was used in the experiments. Acetonitrile (ACN) (HPLC grade, water content <30 ppm) was obtained from Fisher Chemical (USA). *N*,*N*-Dimethylformamide (DMF, AR, 99.5%, water content <0.1%) and dimethyl sulfoxide (DMSO, AR, 99%, water content <0.2%), anhydrous acetonitrile (water content <10 ppm), $CdCl_2{\cdot}2.5H_2O$, $Zn(Ac)_2{\cdot}6H_2O$, NaOH, 5,5-dimethyl-1-pyrroline *N*-oxide (DMPO), oxalic acid (AO), benzoquinone (BQ), sodium azide (NaN_3), butylated hydroxytoluene (BHT), HMF (98%), DFF, FFCA, H_2O_2, $H_2{}^{18}O$, D_2O, benzyl alcohol and its derivatives, 2-pyridinemethanol, 2-thiophenemethanol, cyclohexanol, *etc.*, were all purchased from Aladdin Bio-Chem Technology Co., LTD, Shanghai.

Physical characterization

An X-ray diffractometer (XRD, Rigaku Smartlab) with Cu Kα radiation (λ = 0.154 nm) was used to determine the crystal structure of samples. Energy-dispersive spectrum (EDS) and transmission electron microscopic images (Tecnai G2 F30) were acquired to analyze the morphology of photocatalysts. A UV/vis spectrophotometer (Shimadzu UV-3600) was employed to analyze the photoresponse properties of the catalysts. In order to further study the chemical composition of samples, X-ray photoelectron spectroscopy (XPS, Kratos AXIS NOVA spectrometer) was performed. The Brunauer–Emmett–Teller (BET) method was used to determine the specific surface area.

Sample preparation

In detail, 1.713 g $CdCl_2{\cdot}2.5H_2O$ and 0.549 g $Zn(Ac)_2{\cdot}2H_2O$ were dispersed in 50 mL DI water and stirred for 5 min. After that, 10 mL of 2 M NaOH solution and 1.141 g of thiourea were added into the suspension. Then, the suspension was further stirred for 30 min and transferred into a 100 mL stainless-steel autoclave, maintained at 180 °C for 18 h. Finally, the obtained precipitates were collected and washed. The final products were dried at 60 °C for 6 h. The $Cd_xZn_{1-x}S$ nanoparticles with different elementary ratios were fabricated by using different amounts of $CdCl_2{\cdot}2.5H_2O$ and $Zn(Ac)_2{\cdot}2H_2O$.

For loading different metal co-catalysts: 100 mg $Cd_{0.5}Zn_{0.5}S$ nanoparticles were dispersed into 40 mL water containing 50 μL of 2 M NaOH. After ultrasonication for 30 min, certain amounts of $Co(NO_3)_2{\cdot}6H_2O$, $Ni(NO_3)_2{\cdot}6H_2O$, $Cu(NO_3)_2$, $PdCl_2$, $AgNO_3$, $HAuCl_4$, and H_2PtCl_6 solution were added into the suspension and stirred for 15 min. Subsequently, 10 mL fresh $NaBH_4$ (2 M) solution was added into the suspension dropwise, and after further stirring for 30 min, the obtained green suspension was centrifuged and dried in vacuum.

Photocatalytic HMF oxidation

The photocatalytic HMF oxidation was carried out using a photochemical reactor equipped with 445 ± 10 nm LED (20 W). Typically, 20 mg catalyst was dispersed in a 15 mL quartz tube containing 10 mL reaction solution with an HMF concentration of 10 mM (unless otherwise noted). A mixed solution of water and ACN (HPLC-grade ACN with a H_2O content of 30 ppm was employed unless stated otherwise) was used as the reaction solution (V_{ACN} + V_{H_2O} = 10 mL), in which the water addition volume was controlled to be 0.02 mL, 0.04 mL, 0.08 mL, 0.16 mL, 0.20 mL, 0.30 mL, 0.50 mL, 0.75 mL, 1.70 mL, 2.30 mL, 3.3 mL, 5.0 mL, 7.0 mL, 9.0 mL, and 10.0 mL. After ultrasonic treatment for 4 min, the suspension was employed under air atmosphere for the reaction, and sampling was carried out after a certain reaction time. The other solvents (DMF, DMSO, and water) were also employed for comparison under air atmosphere. For different atmospheres, the air in the reactor was extracted first using a vacuum pump, and then N_2 or O_2 was injected.

For other alcohol substrates and catalysts, the procedures were the same as above HMF oxidation except that different feedstocks were added in the reaction solution of 10 mL ACN or ACN + H_2O.

$$\text{Product yield} = (\text{amount of specific product}/\text{initial amount of HMF}) \times 100\%$$

$$\text{HMF conversion} = (\text{initial amount of HMF} - \text{residual amount of HMF})/\text{initial amount of HMF} \times 100\%,$$

$$\text{Mineralization percentage} = (\text{initial amount of HMF} - \text{overall number of detected products})/\text{initial amount of HMF} \times 100\%.$$

Product quantification

High-performance liquid chromatography (HPLC) was performed using WATERS 2695 equipped with an ultraviolet-visible detector for the quantification of HMF, DFF, FFCA and FDCA (Wavelength: 248 nm; Column: Bio-Rad, Aminex HXP-87P; Mobile phase: 5 mM H_2SO_4; Flow rate: 0.6 mL min^{-1}). For other alcohol substrates, Agilent 7890A equipped with an FID detector and gas chromatograph–mass spectrometer (GC–MS, GC 7890A/5975C inert XL MSD) were used for quantification. The possible gas product through the photocatalytic process was quantified by gas chromatography (Agilent 7890 equipped with a Molecular Sieve packed column and a thermal conductivity detector). The identification and quantification of the products were carried out *via* the calibration curves by applying standard solutions with known concentrations of commercially purchased pure reactants, intermediates, and products.

The produced H_2O_2 was quantified by a reagent color-developing method. First, 1 mL filtered reaction solution was attenuated by 2 mL DI water; after that, 1 mL of the attenuated sample was added into a mixed solution of 1 mL KI (0.4 M) aqueous solution and 1 mL commercial pH buffer with pH = 4 (potassium biphthalate). Finally, the solution was kept for 1 h in the darkness. The H_2O_2 concentration can be determined by the triiodide anion (I_3^-) concentration according to the following equation, where I_3^- can be estimated by Lambert–Beer's law due to their strong absorbance at 350 nm.

Author contributions

Wenhua Xue: conceptualization, formal analysis, investigation, methodology, writing – original draft. Jian Ye: software, resources, visualization. Zhi Zhu: resources, software, validation. Reeti Kumar: data curation, validation. Jun Zhao: conceptualization, investigation, supervision, writing – review & editing.

Data availability

The data supporting this article have been included in this article or as part of the ESI.†

Conflicts of interest

The authors declare no competing interests.

Acknowledgements

This work was supported by the General Research Fund of the University Grants Committee (grant no. 12202723), National Natural Science Foundation of China (NSFC 21908184).

References

1 N. Luo, T. Montini, J. Zhang, P. Fornasiero, E. Fonda, T. Hou, W. Nie, J. Lu, J. Liu, M. Heggen, L. Lin, C. Ma, M. Wang, F. Fan, S. Jin and F. Wang, *Nat. Energy*, 2019, **4**, 575–584.
2 D. Wakerley, M. Kuehnel, K. Orchard, K. Ly, T. Rosser and E. Reisner, *Nat. Energy*, 2017, **2**, 17021.
3 H. G. Cha and K. Choi, *Nat. Chem.*, 2015, **7**, 328–333.
4 Z. Huang, N. Luo, C. Zhang and F. Wang, *Nat. Rev. Chem.*, 2022, **6**, 197–214.
5 J. DiMeglio, A. Breuhaus-Alvarez, S. Li and B. Bartlett, *ACS Catal.*, 2019, **9**, 5732–5741.
6 X. Tan, S. Si, D. Xiao, X. Bao, K. Song, Z. Wang, Y. Liu, Z. Zheng, P. Wang, Y. Dai, B. Huang and H. Cheng, *ACS Catal.*, 2023, **13**, 14395–14403.
7 E. García-López, F. Arcidiacono, A. Vincenzo, L. Palmisano, P. Meo and G. Marcì, *Photochem. Photobiol. Sci.*, 2023, **22**, 1517–1526.
8 M. Zhang, Z. Li, X. Xin, J. Zhang, Y. Feng and H. Lv, *ACS Catal.*, 2020, **10**, 14793–14800.
9 A. Kumar and R. Srivastava, *ACS Appl. Nano Mater.*, 2021, **4**, 9080–9093.
10 H. Zhao, D. Trivedi, M. Roostaeinia, X. Yong, J. Chen, P. Kumar, J. Liu, B. Su, S. Larter, M. Kibria and J. Hu, *Green Chem.*, 2023, **25**, 692–699.
11 Y. Guo, B. Liu, J. Zhang, G. Wang, C. Pan, H. Zhao, C. Wang, F. Yu, Y. Dong and Y. Zhu, *Appl. Catal., B*, 2024, **340**, 123217.
12 L. Yin, Y. Wu, X. Bao, X. Liu, D. Dai, M. Zhang, Z. Wang, Z. Zheng, Y. Liu, H. Cheng, Y. Dai, B. Huang and P. Wang, *Chem. – Eur. J.*, 2023, **29**, e202300999.
13 B. Yang, W. Hu, F. Wan, C. Zhang, Z. Fu, A. Su, M. Chen and Y. Liu, *Chem. Eng. J.*, 2020, **396**, 125345.
14 Y. Yang and T. Mu, *Green Chem.*, 2021, **23**, 4228–4254.
15 C. Li, J. Li, L. Qin, P. Yang and D. Vlachos, *ACS Catal.*, 2021, **11**, 11336–11359.
16 C. Toe, C. Tsounis, J. Zhang, H. Masood, D. Gunawan, J. Scott and R. Amal, *Energy Environ. Sci.*, 2021, **14**, 1140–1175.
17 T. Simon, N. Bouchonville, M. Berr, A. Vaneski, A. Adrović, D. Volbers, R. Wyrwich, M. Döblinger, A. Susha, A. Rogach, F. Jäckel, J. Stolarczyk and J. Feldmann, *Nat. Mater.*, 2014, **13**, 1013–1018.
18 H. Huang, Z. Fang, K. Yu, J. Lü and R. Cao, *J. Mater. Chem. A*, 2020, **8**, 3882–3891.
19 J. Cheng, L. Liu, G. Liao, Z. Shen, Z. Tan, Y. Xing, X. Li, K. Yang, L. Chen and S. Liu, *J. Mater. Chem. A*, 2020, **8**, 5890–5899.
20 Y. Zhu, Y. Zhang, L. Cheng, M. Ismael, Z. Feng and Y. Wu, *Adv. Powder Technol.*, 2020, **31**, 1148–1159.
21 T. Xia, W. Gong, Y. Chen, M. Duan, J. Ma, X. Cui, Y. Dai, C. Gao and Y. Xiong, *Angew. Chem., Int. Ed.*, 2022, **61**, e202204225.
22 N. Pfriem, P. Hintermeier, S. Eckstein, S. Kim, Q. Liu, H. Shi, L. Milakovic, Y. Liu, G. Haller, E. Baráth, Y. Liu and J. Lercher, *Science*, 2021, **372**, 952–957.
23 Z. Liu, E. Huang, I. Orozco, W. Liao, R. M. Palomino, N. Rui, T. Duchoň, S. Nemšák, D. Grinter, M. Mahapatra, P. Liu, J. Rodriguez and S. Senanayake, *Science*, 2020, **368**, 513–517.
24 M. Mellmer, C. Sanpitakseree, B. Demir, P. Bai, K. Ma, M. Neurock and J. Dumesic, *Nat. Catal.*, 2018, **1**, 199–207.

25 J. Saavedra, H. Doan, C. Pursell, L. Grabow and B. Chandler, *Science*, 2014, **345**, 1599–1602.
26 J. Adams, A. Chemburkar, P. Priyadarshini, T. Ricciardulli, Y. Lu, V. Maliekkal, A. Sampath, S. Winikoff, A. Karim, M. Neurock and D. Flaherty, *Science*, 2021, **371**, 626–632.
27 H. Sun, R. Xu, X. Jia, Z. Liu, H. Chen and T. Lu, *Biomass Convers. Biorefin.*, 2023, 1–18.
28 Y. Jiang, S. Li, S. Wang, Y. Zhang, C. Long, J. Xie, X. Fan, W. Zhao, P. Xu, Y. Fan, C. Cui and Z. Tang, *J. Am. Chem. Soc.*, 2023, **145**, 2698–2707.
29 D. Zhang, P. Wang, J. Wang, Y. Li, Y. Xia and S. Zhan, *Proc. Natl. Acad. Sci. U. S. A.*, 2021, **118**, e2114729118.
30 B. Zope, D. Hibbitts, M. Neurock and R. Davis, *Science*, 2010, **30**, 74–78.
31 G. Litwinienko and K. Ingold, *Acc. Chem. Res.*, 2007, **40**, 222–230.
32 S. Mitroka, S. Zimmeck, D. Troya and J. Tanko, *J. Am. Chem. Soc.*, 2010, **132**, 2907–2913.
33 Z. Gao, J. Mu, J. Zhang, Z. Huang, X. Lin, N. Luo and F. Wang, *J. Am. Chem. Soc.*, 2022, **144**, 18986–18994.
34 L. Luo, W. Chen, S. Xu, J. Yang, M. Li, H. Zhou, M. Xu, M. Shao, X. Kong, Z. Li and H. Duan, *J. Am. Chem. Soc.*, 2022, **144**, 7720–7730.
35 Y. Nosaka and A. Nosaka, *Chem. Rev.*, 2017, **117**, 11302–11336.
36 H. Saito and Y. Nosaka, *Catal. Commun.*, 2015, **61**, 117–120.
37 G. Szijjártó, Z. Pászti, I. Sajó, A. Erdőhelyi, G. Radnóczi and A. Tompos, *J. Catal.*, 2013, **305**, 290–306.
38 Q. Liu, J. Lin, H. Cheng, L. Wei and F. Wang, *Angew. Chem., Int. Ed.*, 2023, **62**, e202218720.
39 V. Augugliaro, H. Kisch, V. Loddo, M. López-Muñoz, C. Márquez-Álvarez, G. Palmisano, L. Palmisano, F. Parrino and S. Yurdakal, *Appl. Catal., A*, 2008, **349**, 189–197.
40 K. Sun, X. Wu, Z. Zhuang, L. Liu, J. Fang, L. Zeng, J. Ma, S. Liu, J. Li, R. Dai, X. Tan, K. Yu, D. Liu, W. Cheong, A. Huang, Y. Liu, Y. Pan, H. Xiao and C. Chen, *Nat. Commun.*, 2022, **13**, 6260.
41 Q. Sun, N. Oliveira, S. Kwon, S. Tyukhtenko, J. Guo, N. Myrthil, S. Lopez, I. Kendrick, S. Mukerjee, L. Ma, S. Ehrlich, J. Li, W. Goddard III, Y. Yan and Q. Jia, *Nat. Energy*, 2023, **8**, 859–869.
42 C. Meng, K. Yang, X. Fu and R. Yuan, *ACS Catal.*, 2015, **5**, 3760–3766.
43 T. Wang, Y. Zhang, B. Huang, B. Cai, R. Rao, L. Giordano, S. Sun and Y. Shao-Horn, *Nat. Catal.*, 2021, **4**, 753–762.

